

# Large Exchange Coupling Between Localized Spins and Topological Bands in Magnetic Topological Insulator $\text{MnBi}_2\text{Te}_4$

*Hari Padmanabhan\**, Vladimir A. Stoica, Peter K. Kim, Maxwell Poore, Tiannan Yang, Xiaozhe Shen, Alexander H. Reid, Ming-Fu Lin, Suji Park, Jie Yang, Huaiyu (Hugo) Wang, Nathan Z. Koocher, Danilo Puggioni, Alexandru B. Georgescu, Lujin Min, Seng Huat Lee, Zhiqiang Mao, James M. Rondinelli, Aaron M. Lindenberg, Long-Qing Chen, Xijie Wang, Richard D. Averitt, John W. Freeland, and Venkatraman Gopalan\*

Dr. Hari Padmanabhan, Dr. Vladimir A. Stoica, Dr. Tiannan Yang, Huaiyu Wang, Lujin Min, Prof. Long-Qing Chen, Prof. Venkatraman Gopalan

Department of Materials Science and Engineering, The Pennsylvania State University, University Park, PA 16802, USA

Email: hari@psu.edu, vgopalan@psu.edu

Peter K. Kim, Maxwell Poore, Prof. Richard D. Averitt

Department of Physics, University of California San Diego, La Jolla, CA 92093, USA

Dr. Xiaozhe Shen, Dr. Alexander H. Reid, Dr. Ming-Fu Lin, Dr. Suji Park, Dr. Jie Yang, Dr. Xijie Wang

SLAC National Accelerator Laboratory, Menlo Park, CA 94025, USA

Nathan Z. Koocher, Dr. Danilo Puggioni, Dr. Alexandru B. Georgescu, Prof. James M. Rondinelli

Department of Materials Science and Engineering, Northwestern University, Evanston, IL 60208, USA

This article has been accepted for publication and undergone full peer review but has not been through the copyediting, typesetting, pagination and proofreading process, which may lead to differences between this version and the [Version of Record](https://onlinelibrary.wiley.com/doi/10.1002/adma.202202841). Please cite this article as [doi: 10.1002/adma.202202841](https://onlinelibrary.wiley.com/doi/10.1002/adma.202202841).

This article is protected by copyright. All rights reserved.

Dr. Seng-Huat Lee, Prof. Zhiqiang Mao

2D Crystal Consortium, Materials Research Institute, The Pennsylvania State University, University Park, PA 16802, USA

Department of Physics, Penn State University, University Park, PA 16802, USA

Prof. Aaron Lindenberg

Department of Materials Science and Engineering, Stanford University, Menlo Park, CA 94305, USA

Dr. John W. Freeland

Argonne National Laboratory, Lemont, IL 60439, USA

**Keywords:** magnetic topological materials, itinerant magnetism, ultrafast optics, nonequilibrium, exchange coupling

Magnetism in topological materials creates phases exhibiting quantized transport phenomena with potential technological applications. The emergence of such phases relies on strong interaction between localized spins and the topological bands, and the consequent formation of an exchange gap. However, this remains experimentally unquantified in intrinsic magnetic topological materials. Here, this interaction is quantified in  $\text{MnBi}_2\text{Te}_4$ , an intrinsic antiferromagnetic topological insulator. To achieve this, a multimodal ultrafast approach is employed to interrogate optically induced nonequilibrium spin dynamics. Momentum-resolved ultrafast electron scattering and magneto-optic measurements show that Bi-Te *p*-like states comprising the bulk topological bands demagnetize via electron-phonon scattering at picosecond timescales. Localized Mn *3d* spins, probed by ultrafast resonant X-ray scattering, are found to disorder concurrently with the *p*-like spins, despite being

energetically decoupled from the optical excitation. These results, together with atomistic simulations, reveal that the exchange coupling between localized spins and the bulk topological bands is at least 100 times larger than the primary superexchange interaction, implying an optimal exchange gap of at least 25 meV in the topological surface states. By directly quantifying this exchange coupling, the study validates the materials-by-design strategy of utilizing localized magnetic order to create and manipulate magnetic topological phases, spanning static to ultrafast timescales.

## 1. Introduction

Magnetic order in functional quantum materials provides a rich platform for the discovery of cooperative phenomena with potential applications in magnetic memory, dissipationless electronics, spintronics, quantum computing, and more. These phenomena arise out of interaction between magnetic order and other functional microscopic degrees of freedom. This is exemplified in the  $\text{Mn}(\text{Bi,Sb})_{2n}\text{Te}_{3n+1}$  family of materials, which is the first realization of intrinsic magnetic order in a topological insulator.<sup>[1–6]</sup> The band topology is intimately connected to magnetism, with experimental demonstration of quantum anomalous Hall and axion insulator phases,<sup>[7–9]</sup> and magnetic field-driven topological phase transitions.<sup>[3,8]</sup> While the magnetic order is due to localized Mn 3d spins, it is the exchange coupling between the localized spins and the topological bands,<sup>[10]</sup> and the resultant formation of an exchange gap in the topological surface states that is responsible for the above phenomena.

The inverted topological bands in  $\text{Mn}(\text{Bi,Sb})_{2n}\text{Te}_{3n+1}$  are comprised of bulk  $p$ -like Bi/Sb and Te states.<sup>[11]</sup> The exchange gap  $\Delta$  induced in the corresponding topological surface states by magnetic order can be written in the form (see **Figure 1a**)

$$\Delta = J_{pd}\bar{S}_z, \quad (1)$$

where  $\bar{S}_z$  is the average projection of Mn  $3d$  localized spins along the normal to the surface and  $J_{pd}$  is the exchange coupling between localized Mn  $3d$  spins and the  $p$ -like states that comprise the topological bands.<sup>[10,12–14]</sup> The exchange gap  $\Delta$  has been measured by angle-resolved photoemission spectroscopy (ARPES),<sup>[1,15,16]</sup> whereas the bulk and surface magnetic properties have been characterized using a variety of experimental techniques including magnetometry,<sup>[17,18]</sup> neutron scattering,<sup>[17,19,20]</sup> and magnetic force microscopy<sup>[21,22]</sup>. On the other hand, despite its outsized influence on magnetic topological phenomena,  $J_{pd}$  remains experimentally unquantified. Magnon dispersion measured by inelastic neutron scattering may allow experimental access to such interatomic exchange couplings, but the absence of a discernible  $p$ -like magnetic moment makes such an approach infeasible.<sup>[17]</sup> Magneto-transport measurements have been used to estimate such interactions in dilute magnetic semiconductors through the effects of carrier-spin scattering.<sup>[23,24]</sup> However, this is an indirect probe that relies on simplifying assumptions on exchange interactions which do not hold in intrinsic magnetic materials. Such indirect approaches may furthermore be obscured by other interactions such as magnetodielectric coupling.<sup>[25]</sup> As a consequence, no experimental quantification of  $J_{pd}$  and its influence on magnetic dynamics has been reported on the  $\text{Mn}(\text{Bi,Sb})_{2n}\text{Te}_{3n+1}$  family of materials, or indeed any intrinsic magnetic topological material.

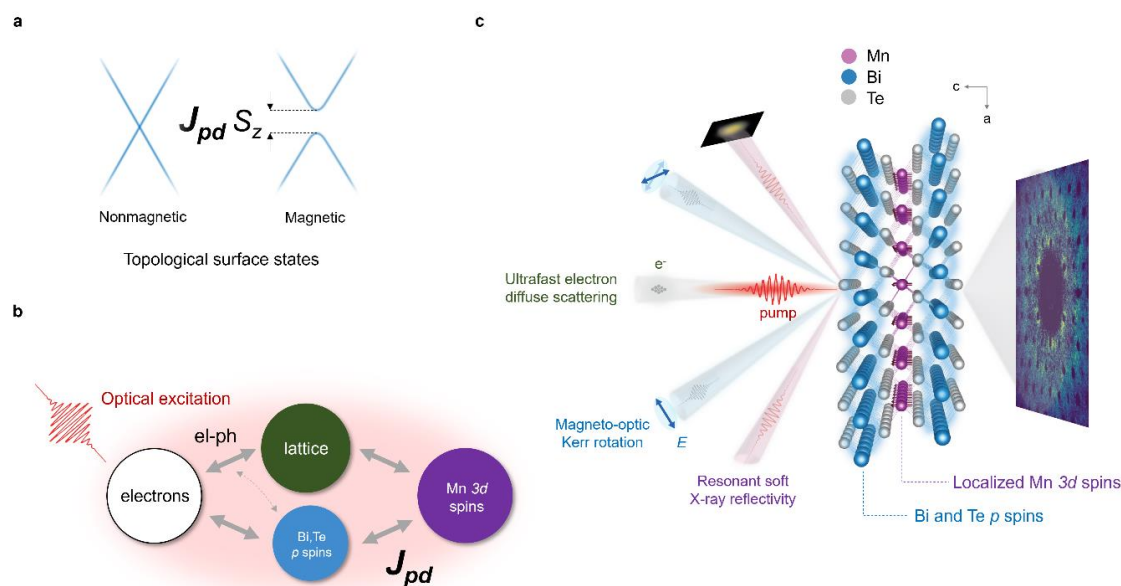


**Figure 1 Multimodal probe of ultrafast magnetic dynamics to determine  $J_{pd}$ .** **a**, Schematic of the  $p$ -like topological surface states in  $\text{MnBi}_2\text{Te}_4$ , with the exchange gap given by  $J_{pd} S_z$ , where  $J_{pd}$  is the  $p$ - $d$  exchange coupling and  $S_z$  is the projection of Mn 3d localized spins along the  $c$  direction. **b**, Schematic illustrating the interplay between nonequilibrium electronic, spin, and lattice dynamics in  $\text{MnBi}_2\text{Te}_4$ , with  $J_{pd}$  highlighted. **c**, Schematic illustrating the time-resolved experimental probes used to characterize nonequilibrium dynamics in  $\text{MnBi}_2\text{Te}_4$ . The crystal lattice structure of  $\text{MnBi}_2\text{Te}_4$  is shown with the  $p$  spins illustrated schematically by blue clouds, and localized  $d$  spins illustrated by arrows on Mn ions. Ultrafast electron diffuse scattering is used to probe electron-phonon coupling. Time-resolved magneto-optic Kerr rotation (with the polarization of the optical electric field  $E$  illustrated using blue arrows) is used to probe dynamics of Bi-Te  $p$  spins. Time-resolved resonant soft X-ray scattering at the Mn  $L$ -edge is used to probe dynamics of localized Mn  $d$  spins.

The quantification of  $J_{pd}$  is especially critical in light of the debate over the exchange gap in the topological surface states (TSS) in  $\text{MnBi}_2\text{Te}_4$  and related materials. While some transport experiments reveal signatures of quantized behavior due to magnetism,<sup>[7,8]</sup> these occur at temperatures well below the magnetic ordering temperature. Importantly, a wide spectrum of contradictory results are reported on the exchange gap in the TSS measured by ARPES, despite the

well-established bulk magnetic order. Initial papers on  $\text{MnBi}_2\text{Te}_4$  reported a large exchange gap upto 100 meV in the TSS.<sup>[1,18,26]</sup> However this gap was reported to be independent of temperature, with the magnitude remaining unchanged from 10 K to 300 K,<sup>[1,18]</sup> raising questions about its magnetic origin. Subsequently several papers, using a combination of laser- and synchrotron-based ARPES measurements reported that the TSS in  $\text{MnBi}_2\text{Te}_4$  are actually gapless.<sup>[15,16,27,28]</sup> Some of these papers argued that the earlier reports of a large exchange gap were due to a misidentification of bulk bands. A systematic study of the exchange gap in the presence of sample-dependent variations, vacancies and substitutional defects, variance in cleavage planes, and uncompensated charge was carried out in more recent work.<sup>[29–31]</sup> These studies reported that the exchange gap can vary from <5 meV to >60 meV, dependent on the above variations, intrinsic to even high-quality crystals. Apart from this, the main arguments used to rationalize the discrepancy in the literature are a possible reconstruction of magnetic order at the surface,<sup>[15]</sup> nanometer scale magnetic domains,<sup>[16]</sup> and vanishingly weak  $J_{pd}$  exchange coupling.<sup>[21,27]</sup>

The literature review above highlights the importance of directly experimentally evaluating  $J_{pd}$ , a key parameter in the formation of the exchange gap. Such a quantification would provide important information complementary to existing ARPES studies that directly measure the gap  $\Delta$ , and bulk- and surface-sensitive magnetic techniques that measure  $S_z$ .

Rather than rely on measurements of the exchange gap to estimate  $J_{pd}$ , we use an alternative approach, previously demonstrated on elemental ferromagnets and their alloys, such as Gd, Tb, and GdFeCo.<sup>[32–34]</sup> We interrogate  $J_{pd}$  in  $\text{MnBi}_2\text{Te}_4$  by optically driving the system out of equilibrium and measuring the magnetic response at its intrinsic timescales, as shown in the schematic in Fig. 1b. Ultrafast optical excitation is used to create hot carriers, which thermalize with the lattice and spins

through various processes and subsequently melt the magnetic order. We employ a multimodal ultrafast probe (see Figure 1c) to unambiguously characterize the nonequilibrium spin dynamics and their interplay with electrons and the lattice. Ultrafast electron diffuse scattering in combination with time-resolved magneto-optic Kerr effect measurements reveal clear signatures of spin-polarization in the Bi and Te *p*-like states comprising the bulk topological bands, which disorder through electron-phonon spin-flip scattering at picosecond timescales. Localized Mn *3d* spins, probed through time-resolved resonant soft X-ray scattering, despite being located far below the Fermi level and energetically decoupled from the initial optical excitation, are observed to disorder concurrently with the *p* spins. In the absence of hot carriers which demagnetize the *p* spins, the localized spins instead melt at orders-of-magnitude slower rates via thermalization with the lattice. The above observations suggest that the Mn *3d* localized spins and *p*-like bulk topological bands are coupled by a strong interatomic exchange coupling  $J_{pd}$ . Modeling our experimental results using orbital-resolved atomistic Landau-Lifshitz-Gilbert (LLG) simulations, we estimate that  $J_{pd}$  is at least 100 times larger than the in-plane superexchange coupling. This estimate implies that with pristine magnetic order, the topological surface states should exhibit an exchange gap of at least 25 meV. Our multimodal measurement of ultrafast magnetic dynamics in MnBi<sub>2</sub>Te<sub>4</sub> thus sheds light on the exchange pathways that enable magnetic topological phases and provides a foundation for the manipulation of spin-based phenomena interfaced with band topology.

## 2. Results

We synthesized high-quality crystals of MnBi<sub>2</sub>Te<sub>4</sub> using a flux-growth technique. Our material characterization work using X-ray diffraction, magneto-transport measurements, magnetometry,

Raman spectroscopy, and ARPES can be found in the SI Section S1 and our previous publications.<sup>[3,18,28,35]</sup> Below, we focus on our multimodal ultrafast investigation.

The penetration depth of the 1.55 eV optical pulses used in our measurements is 20 nm, which corresponds to 14 septuple layers of  $\text{MnBi}_2\text{Te}_4$ . The TSS have a depth of around 2 septuple layers.<sup>[36]</sup> ARPES measurements show that the Fermi level is  $\sim 0.2$  eV above the conduction band edge,<sup>[18]</sup> resulting in a significant bulk carrier density. Hence our measurements are sensitive to primarily bulk electronic states, with a small contribution from the TSS.

### 2.1. Momentum-resolved probe of electron-phonon scattering

A key ingredient of any description of nonequilibrium magnetic dynamics is the transfer of angular momentum associated with ordered spins into different degrees of freedom. In an ultrafast demagnetization experiment, charge carriers scattering with phonons is hypothesized to be the dominant channel of dissipation of spin angular momentum.<sup>[37–39]</sup> Here, every electron-phonon scattering event is associated with a finite spin-flip probability, where the hot electron provides the energy to flip the spin and the phonon provides the angular momentum. Given this, a complete description of ultrafast magnetic dynamics requires the quantification of electron-phonon coupling and nonequilibrium phonon dynamics. We employ state-of-the-art MeV ultrafast electron diffuse scattering (UEDS) as a direct, momentum and mode-resolved probe of electron-phonon coupling (see schematic in **Figure 2a**). Our results show that hot electrons in  $\text{MnBi}_2\text{Te}_4$  are directly coupled to optical phonons, which subsequently couple to acoustic phonons. In particular, we subsequently show that carrier-optical phonon scattering results in demagnetization via spin-flip processes.



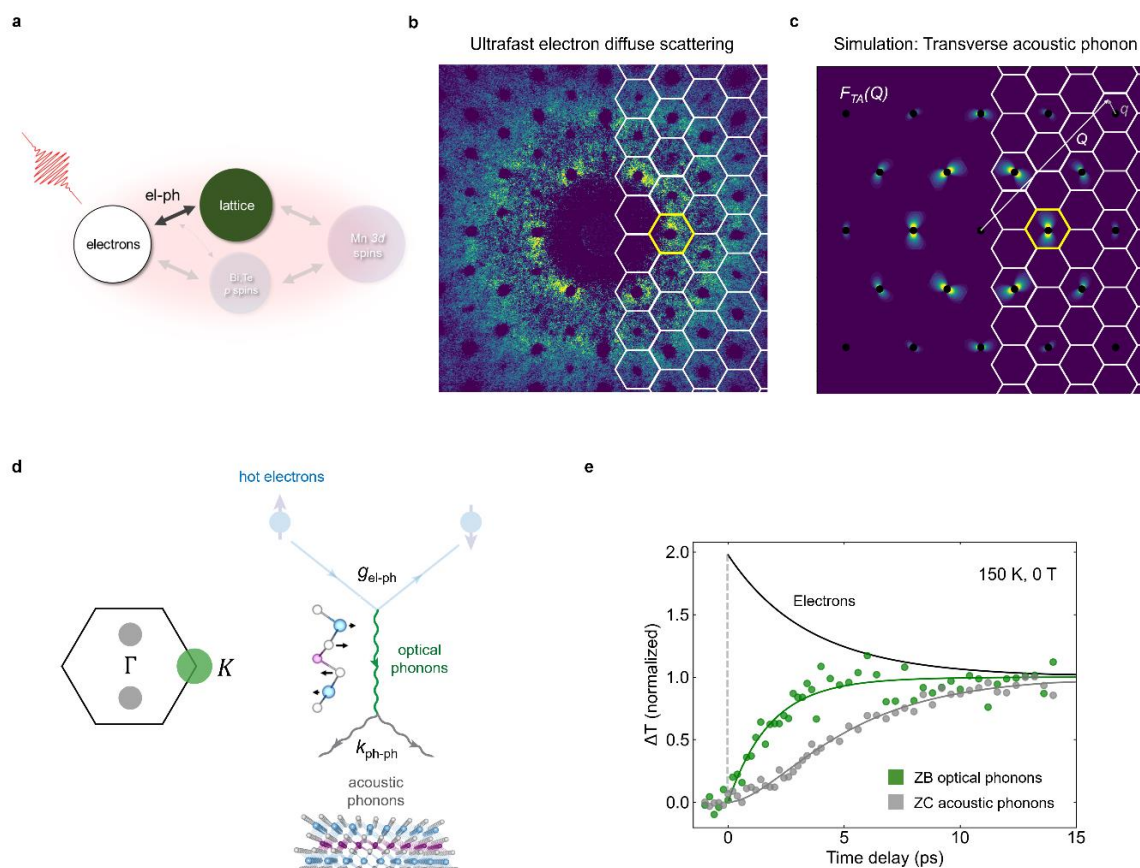


**Figure 2 Momentum-resolved electron-phonon scattering.** **a**, Schematic of the subsystem probed by ultrafast electron diffuse scattering (UEDS). **b**, Snapshot of UEDS, obtained by subtracting the static diffuse scattering from the pump-induced diffuse scattering integrated over time delay  $t > 0$ . **c**, Simulation of the structure factor  $F_{TA}(\mathbf{Q})$  of the transverse acoustic phonon branch, where  $\mathbf{Q}$  is the scattering wavevector. Brillouin zones (BZ) are drawn in white as a guide to the eye in (a) and (b). **d**, (right) Schematic of electron-phonon and phonon-phonon scattering, with the respective coupling constants  $g_{el-ph}$  and  $k_{ph-ph}$ . (left) Regions of integration to obtain optical (green) and acoustic (grey) phonon populations for the BZ highlighted in yellow in (b) and (c). **e**, Experimental phonon populations (circles). These were obtained using the regions of integration shown in (d). The solid lines are fits to the non-thermal model shown schematically in panel (d) (ZB: zone boundary, ZC: zone center).

A snapshot of the ultrafast electron diffuse scattering, obtained by subtracting the static diffuse scattering intensity from the time-integrated intensity at time delays  $t > 0$  is shown in Figure 2b (also see Methods and SI Section S2). Phonon Brillouin zones are overlaid on the scattering phase space as a guide to the eye. A complete mode-resolution of the transient scattering intensity is hindered by the large number of phonons (3 acoustic and 18 optical branches) and their entwined dispersion curves.<sup>[2]</sup> A more informative approach is to separate the acoustic and optical phonon contributions. Acoustic phonons, due to their vanishing frequencies, will dominate the UEDS signal near the zone center (see discussion in SI Section S3). In Figure 2c, we show a simulation of the structure factor  $F_{TA}$  (see SI Section S3 for details) of the transverse acoustic (TA) phonon branch, which exhibits a divergent intensity near the zone-centers with a characteristic azimuthal dependence. Examination of the experimental data in Figure 2b shows a clear signature of this mode. It is noteworthy that there are no signatures of the longitudinal acoustic branch, which has a radial form factor (see SI Section S3 for simulation). Finally, the diffuse scattering intensity in regions where  $F_{TA}$  vanishes may be attributed to optical phonons (see SI Section S2 for a detailed discussion of phonons away from the zone-center). Based on this, we employ regions of integration as shown in the schematic in Figure 2d to isolate the contribution of optical (green) and acoustic (grey) phonons to the diffuse scattering intensity.

We carry out measurements at 150 K and above where transient phonon population changes may be approximated as temperature changes, i. e.  $\Delta n \propto \Delta T$  (see SI Section S4). While this is well above the antiferromagnetic (AFM) ordering temperature  $T_N = 24$  K, we note that electron-phonon coupling is very weakly temperature-dependent in the range of electronic temperatures achieved in our experiments, and in the absence of electronic and structural transitions.<sup>[40–42]</sup> Indeed, as we show below, despite the difference in temperatures, our UEDS measurements are fully consistent with the low-temperature ultrafast magnetic measurements.

The plot in Figure 2e shows the experimental transient zone boundary (ZB) optical phonon and zone center (ZC) acoustic populations converted to normalized temperatures (see SI Section S4) as a function of time delay after pump excitation. In the first two picoseconds, only optical phonons show an appreciable transient population, with acoustic phonons exhibiting a delayed rise. We analyze the results using a nonthermal model of nonequilibrium phonons, consisting of two phonon subsystems (optical and acoustic) individually described by distinct transient temperatures. The pump excitation is assumed to instantaneously create an electronic state with an elevated temperature, which subsequently thermalizes with the lattice by scattering with the two phonon subsystems. The scattering of hot electrons with optical phonons is described by the electron-phonon coupling parameter  $g_{el-ph}$ . The optical phonons decay into acoustic phonons by a phonon-phonon coupling parameter  $k_{ph-ph}$ , as shown in the schematic in Figure 2d. We fit the entire set of temperature-dependent experimental data (see SI Section S4 for details, numerical simulations, and fitting) to a temperature-independent  $g_{el-ph}$  and a variable  $k_{ph-ph}$ . The fit results for experiments at 150 K, plotted as solid lines in Figure 2e, closely follow the experimental results, and correspond to  $g_{el-ph} = 0.27 \times 10^6$  J K<sup>-1</sup> m<sup>-3</sup> ps<sup>-1</sup> and  $k_{ph-ph} = 0.1 \times 10^6$  J K<sup>-1</sup>. Our final fit results are robust, remaining unchanged with one order-of-magnitude variation in the initial fit estimates.

The following observations are made – (i) the experimental data are consistent with a model in which hot electrons couple only to optical phonons, i. e. the fits of the numerical simulations are insensitive to any additional coupling. (ii) The thermalization of the phonon subsystem takes over 5 ps, as opposed to the electron-optical phonon scattering timescale of around 1 ps. (iii) The experimental data are consistent with a temperature-independent  $g_{el-ph}$  (see discussion in SI Section

S4). This is in line with the absence of electronic and structural phase transitions in the measured temperature range.

## 2.2 Disordering of Bi and Te $p$ spins by electron-phonon spin-flip scattering

Our UEDS measurements show that electron-phonon thermalization in  $\text{MnBi}_2\text{Te}_4$  occurs primarily via optical phonons over a timescale of 1 ps. Next, we measure the demagnetization of the states comprising the bulk topological bands due to such electron-optical phonon scattering events (see schematic in **Figure 3a**). The phonon-mediated spin-flip scattering process that causes demagnetization is schematically shown in Figure 3b, where  $a_{sf}$  is the spin-flip probability. In Figure 3c, we show the density of states projected onto atomic orbitals, calculated using density functional theory (DFT) including spin-orbit interaction (see Methods and SI Section S5), of the AFM phase. Localized Mn  $3d$  spins are the dominant spin-polarized bands ( $4.28 \mu_B$ ), however, there is also a small contribution to the magnetic moment from Bi  $5p$  ( $\sim 0.02 \mu_B$ ) and Te  $4p$  ( $\sim 0.03 \mu_B$ ) states that comprise the bulk topological bands (see SI Section S5). While pristine  $\text{MnBi}_2\text{Te}_4$  is an insulator, as-grown crystals are metallic due to defect doping, with the Fermi level ( $E_F$ ) at  $\sim 0.2$  eV above the conduction band edge.<sup>[16,18]</sup> Given the penetration depth of our optical pulses and the Fermi level, these measurements primarily probe the aforementioned bulk Bi and Te  $p$ -like states.

We measure ultrafast demagnetization of  $p$  states due to electron-phonon scattering by employing time-resolved magneto-optic Kerr effect (trMOKE) measurements (see Methods). Our measurements are directly sensitive to optical transitions and spin-polarization in the valence and conduction band. Importantly, the pump does not excite occupied localized Mn  $3d$  states, which are at  $\sim 4$  eV below  $E_F$ , so that only valence and conduction  $p$ -like spins are directly disordered by pump-induced processes. The measurements are carried out at 30 K and at a field of 1 T to induce a static net magnetization ( $\sim 0.3 \mu_B$ ) and finite Kerr rotation  $\theta$ . The transient pump-induced Kerr rotation  $\Delta\theta$  (see SI Section S6 for Kerr ellipticity), plotted in the lower panel of Figure 3d using blue circles (normalized to the maximum demagnetization), shows an ultrafast demagnetization occurring at picosecond timescales. The demagnetization exhibits a characteristic shoulder that also corresponds to the timescale of electron-optical phonon thermalization. These observations are consistent with a disordering of  $p$  spins by electron-phonon spin-flip processes as we show below.

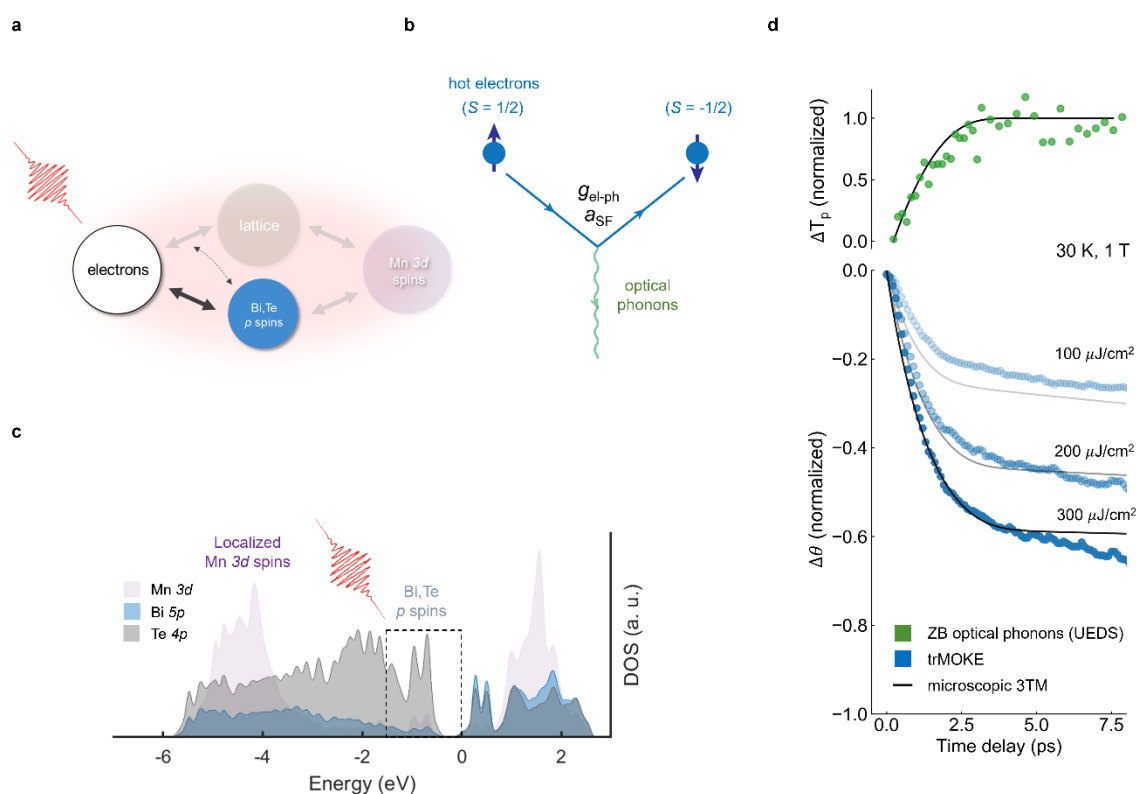


**Figure 3 Disordering of  $p$  spins via electron-phonon spin-flip scattering.** **a**, Schematic of the subsystem probed by time-resolved magneto-optic Kerr effect (trMOKE) measurements. **b**, Schematic of phonon-mediated spin-flip scattering, where  $g$  is the electron-phonon coupling constant, and  $a_{SF}$  is the spin-flip probability. **c**, Atomic-projected density of states of the antiferromagnetic phase of  $\text{MnBi}_2\text{Te}_4$ . Bands with localized  $3d$  and conduction and valence  $p$  spins are indicated. The 1.55 eV pump excitation is schematically shown. **d**, (bottom) Results of trMOKE experiments (blue circles), with pump fluences labeled next to the plots. The black lines are fits to phenomenological model of electron-phonon spin-flip scattering shown schematically in panel (a). (top) Plot of normalized change in optical phonon temperature from UEDS measurements (green circles).

We model the experimental results in Figure 3d using a phenomenological model that considers individual electron-phonon spin-flip scattering events. To start with, we first consider only the  $p$  spin subsystem, ignoring its coupling to localized spins. Following the approach used in the literature,<sup>[43]</sup> we fix various model parameters using experimental inputs and DFT calculations (see SI Section S7). Additionally, we fix the electron-phonon scattering rate  $g_{el-ph}$  to the value obtained from our UEDS measurements, leaving the spin-flip probability  $a_{SF}$  and an effective exchange splitting as the only variables. The equations are solved numerically and fit to the entire fluence-dependent experimental dataset. The fit results are shown using solid black lines in Figure 3d. The following observations can be made – (i) the experimental results show good qualitative agreement with our model of electron-phonon spin-flip scattering, capturing the fluence-independent shoulder near 2 ps, the change in slope across the shoulder, and the overall fluence-dependent scaling. (ii) A spin-flip probability  $a_{SF}$  of 0.06 and an effective exchange splitting of 10 meV are obtained, both of which are physically reasonable values (see SI Section S7 for a discussion).<sup>[39]</sup> (iii) In addition to the timescale of demagnetization, the model predicts the dynamics of phonon populations due to electron-phonon thermalization, denoted in the top panel of Figure 3d using a solid black line. This prediction is in

excellent agreement with the phonon population rate directly measured using UEDS, shown in green, confirming the mutual consistency of the experimental results.

The trMOKE measurements allows for the determination of the timescale of demagnetization of *p*-like spins, and our model of electron-phonon spin-flip scattering provides a good qualitative description of the underlying mechanism. However, this simplified model is subject to two limitations. First, the trMOKE experiments are carried out under a finite magnetic field, rather than in the AFM ground state. Second, the model neglects the exchange coupling  $J_{pd}$  between the *p*-like states and localized Mn 3*d* spins. Though trMOKE is a direct probe of magnetic contrast in the optically accessible Bi and Te *p*-like bands, the localized Mn 3*d* spins can influence these dynamics via  $J_{pd}$ . In the following sections, we measure and quantify this exchange coupling by isolating the dynamics of Mn 3*d* spins in the AFM state.

### 2.3 Demagnetization of localized Mn spins via $J_{pd}$

In order to isolate the dynamics of localized Mn spins (see schematic in **Figure 4a**), we employ time-resolved resonant soft X-ray scattering (trRSXS) at the Mn  $L_3$  edge (corresponding to  $2p \rightarrow 3d$  dipole transitions, see schematic in Figure 4b and Methods). The temperature-dependent static spectra plotted in Figure 4b show that reflectivity at the  $L_3$  edge is sensitive to the AFM order (see SI Section S8 for static temperature-dependence). We carry out pump-probe measurements with a 1.2 eV pump (see Methods) that excites *p* states, and the probe energy fixed at 638 eV to resonantly probe the AFM order of localized Mn spins. In addition, these measurements are carried out at 0 T, and are

thus a direct probe of the AFM order, rather than a polarized paramagnetic state as in the trMOKE measurements.

The trRSXS results are plotted in Figure 4c. Two distinct timescales are observed in the dynamics, with varying amplitudes as a function of fluence. An initial, fast disordering (i. e. melting of AFM order) occurs at timescales below the experimental resolution (probe pulsewidth  $\sim 90$  ps), indicated using dashed lines. This is followed by a slow disordering occurring over hundreds of picoseconds. At sufficiently high fluences ( $\sim 100 \mu\text{J}/\text{cm}^2$ ), the initial fast disordering fully melts the magnetic order. The different timescales and fluence-dependence are suggestive of two distinct mechanisms of disordering of localized Mn  $3d$  spins.

We first consider the slow process. This can be explained as the result of thermalization between the localized Mn  $3d$  spins and the lattice. Making use of a two-temperature model, separating the lattice and localized spin subsystems, the set of fluence-dependent data in the low fluence limit (i. e. where the initial fast demagnetization is negligible) can be fit (solid black lines in Figure 4c) to a single spin-lattice thermalization constant  $g_{sl}$  (see SI Section



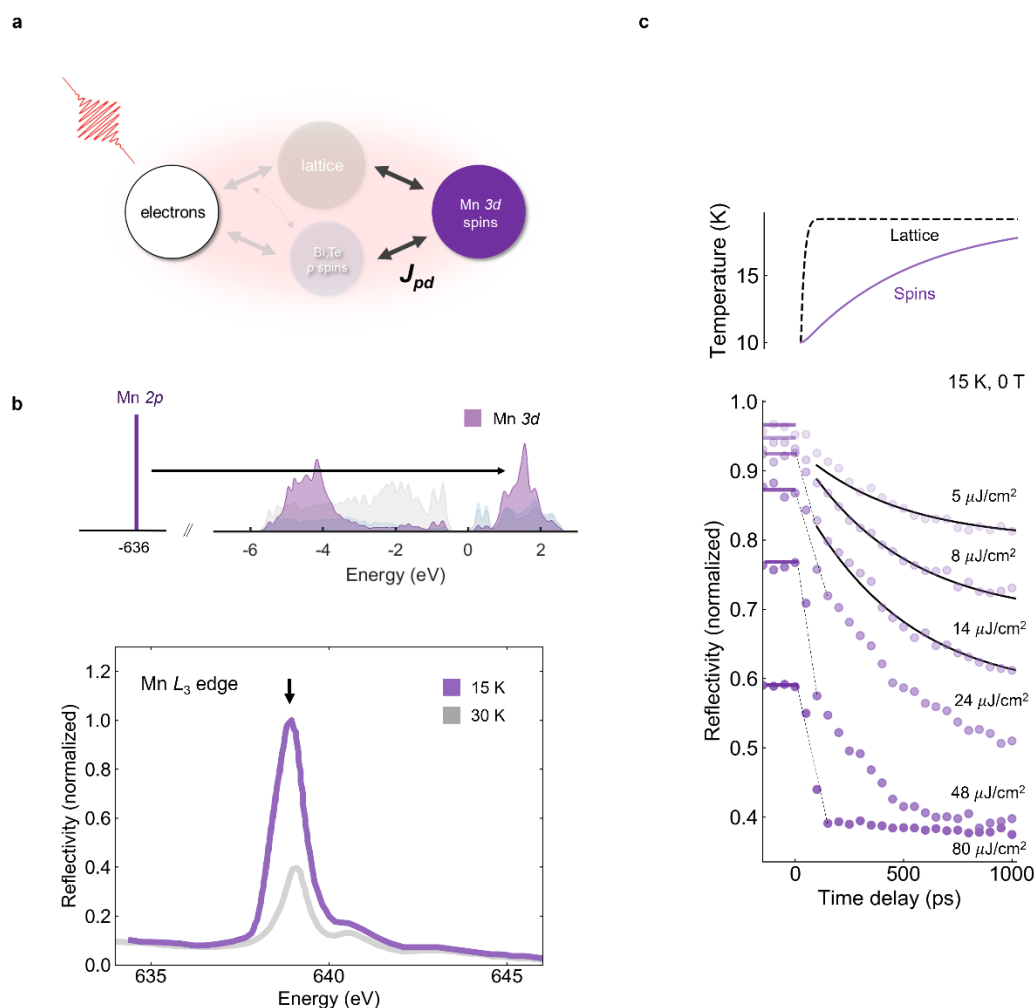


**Figure 4 Disordering of Mn 3d localized spins via  $J_{pd}$ .** **a**, Schematic of the subsystem probed by time-resolved resonant soft X-ray scattering (trRSXS) measurements. **b**, Schematic of resonant optical transition (top), and static RSXS spectrum (bottom). **c**, (bottom) trRSXS results (purple circles) and fit (solid black line) to spin-lattice two-temperature model, with pump fluences labeled next to plots. (top) Spin and lattice temperatures at pump fluence of  $20 \mu\text{J}/\text{cm}^2$  extracted from two-temperature model.

S9). The thermalization process is illustrated by plotting the transient spin and lattice temperatures in the top panel of Figure 4c. While the lattice thermalizes within the first 15 ps (as shown in Figure 2e), the spins are only weakly coupled to the lattice, resulting in a thermalization timescale of the

order of 400 ps. Spin-lattice thermalization occurs due to coupling between the angular momentum of localized  $3d$  spins and thermal lattice motions, mediated by the orbital angular momentum  $L$  via the spin-orbit interaction  $\xi L \cdot S$ . The orbital angular momentum is nominally fully quenched in the Mn  $3d^5$  spin state (i. e.  $L = 0$ ), resulting in a weak coupling of the lattice to Mn spin order, and thus the extremely long thermalization timescales.

The (pulsewidth-limited) fast disordering is at odds with the above discussion. On the other hand, this timescale is consistent with demagnetization via spin-flip scattering observed in the conduction band. This suggests that the localized Mn  $3d$  spins are strongly coupled to Bi and Te  $p$  spins via an interatomic exchange interaction  $J_{pd}$ . In such a scenario, a sufficiently high-fluence pump excitation would completely disorder not just the  $p$  spins, but also the localized  $3d$  spins at timescales comparable to electron-optical phonon scattering. At lower fluences, only a partial disordering of localized  $3d$  spins would occur, allowing for subsequent demagnetization via the slower thermalization process. The results in Figure 4c are completely consistent with the above description. This picture of two distinct demagnetization processes with disparate timescales is true across the different magnetic phases of  $\text{MnBi}_2\text{Te}_4$ , as shown by our temperature-dependent trMOKE measurements (see SI Section S10). The initial fast demagnetization observed in the trRSXS measurements is thus evidence for a strong interatomic exchange interaction  $J_{pd}$  that disorders the Mn  $3d$  localized spins concurrently with the  $p$  spins.

## 2.4 Estimating $J_{pd}$ using Landau-Lifshitz-Gilbert simulations

To provide phenomenological insight into the experimentally observed coupled magnetic dynamics, we consider a Heisenberg-like Hamiltonian describing coupled  $p$  and  $d$  spins, which also forms the microscopic basis for Eq. 1 (see SI Section S13):

$$H = -\sum_{ij} J_d^{ij} \mathbf{S}_d^i \cdot \mathbf{S}_d^j - K_d \sum_i S_d^{zi^2} - J_{pd} \sum_i \mathbf{S}_p^i \cdot \mathbf{S}_d^i. \quad (2)$$

Here,  $\mathbf{S}_d^i$  and  $\mathbf{S}_p^i$  are Mn  $3d$  and Bi-Te  $p$ -like spins at site  $i$ , respectively.  $J_d^{ij}$  is the exchange coupling constant of Mn  $3d$  spins including  $J_{d,IP}$  for nearest-neighbor in-plane spins and  $J_{d,OOP}$  for nearest-neighbor out-of-plane neighbors,  $K_d$  is the single-ion anisotropy coefficient,  $S_d^{zi}$  is the  $z$ -component of  $\mathbf{S}_d^i$ , and  $J_{pd}$  is the intra-atomic exchange interaction between Mn  $3d$  spins and Bi/Te  $p$  spins. Since  $|S_p/S_d| \sim 0.01$ , we neglect terms of the order  $S_p^2$ .

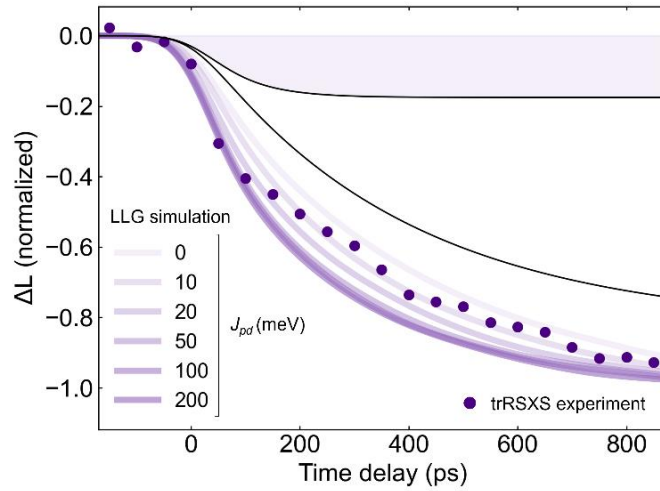


**Figure 5 Estimating  $J_{pd}$  using LLG simulations.** The pump-induced change in the antiferromagnetic order parameter  $L$  corresponding to Mn  $3d$  spins is plotted, with circles denoting results from time-resolved resonant soft X-ray scattering (trRSXS) measurements at a pump fluence of  $29 \mu\text{J}/\text{cm}^2$ , and solid purple lines denoting results of Landau-Lifshitz-Gilbert (LLG) simulations as a function of the interatomic exchange coupling  $J_{pd}$ . The black lines are the individual exponential decay functions used to fit the simulation results for  $J_{pd} = 20 \text{ meV}$ . The purple region highlights the disordering of spins achieved due to  $J_{pd}$ . The simulation results are convoluted with a 90 ps Gaussian to model the experimental probe pulsewidth.

Based on the above ratio of the magnitudes of  $p$  and  $d$  spins,  $J_{pd}$  must have a value at least 100 times larger than  $J_d$  in order for the last term to have a significant contribution to the magnetic dynamics, as indicated by the concurrent  $p$ - $d$  demagnetization observed in our measurements. Using  $J_d = 0.12$  meV extracted from inelastic neutron scattering,<sup>[19]</sup> we can estimate that  $J_{pd}$  must be at least 10 meV.

To substantiate these arguments, we employ orbital-resolved atomistic Landau-Lifshitz-Gilbert simulations (see Methods for details). Here nonequilibrium spin dynamics are determined by means of the spin Hamiltonian, along with orbital-resolved phenomenological ‘damping’ terms  $\alpha_p$  and  $\alpha_d$  that couple the  $p$  and  $d$  spin dynamics to the electronic and lattice heat baths, respectively. We use previously reported experimental results to fix the values of  $J_{d,IP}$ ,  $J_{d,OOP}$ ,  $K_d$ , and  $\mathbf{S}_d$ ,<sup>[17,19]</sup> (see SI Section S11 for values) and estimate  $\mathbf{S}_p$  using density functional theory calculations (see SI Section S5). We find good agreement between the simulated Mn  $3d$  spin dynamics and the experimental trRSXS results using  $\alpha_d = 0.003$  and  $\alpha_p = 0.5$ , with  $J_{pd}$  in the range of 10-50 meV.

In particular, the simulations accurately reproduce the static ordering temperature  $T_N = 24$  K (see Figure S9a), and in the limit of  $J_{pd} = 0$ , the low fluence spin-lattice thermalization dynamics (see Figure S9b). In **Figure 5**, we compare the experimental Mn  $3d$  demagnetization at an intermediate fluence ( $29 \mu\text{J}/\text{cm}^2$ ) with the results of our LLG simulations for various values of  $J_{pd}$ . The results show that a value of  $J_{pd} > 10$  meV is necessary to reproduce the experimentally observed initial fast demagnetization step. The simulated dynamics are well-described by a bi-exponential decay function, a representative sample of which is shown for  $J_{pd} = 20$  meV. The dynamics consist of a fast step with a time constant of  $\sim 70$  ps (black line with purple shading) corresponding to the disordering of Mn  $3d$  spins due to its coupling to  $p$  spins via  $J_{pd}$ , and a slow step (black line) with a time constant

This article is protected by copyright. All rights reserved.

of ~380 ps corresponding to spin-lattice thermalization (also see Figure S9b). The time constant of the fast step is consistent with the pulsewidth-limited disordering observed in our experiments.

We have quantified  $J_{pd}$  above by measurement of localized Mn  $3d$  and Bi-Te  $p$ -like states comprising the bulk topological bands. That the bulk  $J_{pd}$  evaluated here is of direct consequence to the  $p$ -like TSS can be illustrated using a minimal theoretical model. In SI Section S12, we construct a slab model starting from the Bernevig-Hughes-Zhang Hamiltonian,<sup>[44]</sup> a prototype used to describe topological insulators. We model the effect of local magnetic order by means of an additional Zeeman term proportional to  $J_{pd}$ . The calculated band structure shows that a single exchange parameter, coupling localized spins to the bulk and surface  $p$ -like states in an identical manner, fully reproduces the characteristic phenomenology of a magnetic topological insulator, namely the formation of an exchange gap in the TSS and a quantized Hall conductivity. The value of  $J_{pd}$  evaluated in our study is thus a good, quantitative estimate of the exchange coupling between localized Mn  $3d$  spins and the  $p$ -like TSS.

It is also of interest to determine the mechanism underlying  $J_{pd}$ . The calculated bulk band structure in Fig. 3e shows that the  $p$  spin subsystem in as-grown  $\text{MnBi}_2\text{Te}_4$  consists of both valence and conduction states. Hence,  $J_{pd}$  may be the result of localized Mn  $3d$  spins coupling to valence electrons by the Van Vleck susceptibility, coupling to conduction electrons by the Ruderman-Kittel-Kasuya-Yosida (RKKY) mechanism, or both.<sup>[14,45,46]</sup> Both the valence and conduction  $p$  states are excited and probed in our experiments, precluding the unambiguous resolution of a dominant mechanism. This may be achieved by a systematic study as a function of Sb doping and electrostatic gating.<sup>[47]</sup> A dominant Van Vleck mechanism would imply that  $J_{pd}$  is independent of bulk carrier density and the Fermi level. An RKKY-like mechanism would imply a dependence on bulk carrier

density and the Fermi level, with a particularly interesting scenario arising at the Dirac point, since the TSS form an itinerant system at the surface.<sup>[48]</sup>

### 3. Conclusion

The transfer of spin angular momentum is a critical aspect of ultrafast magnetic dynamics. Our work demonstrates the role played by optical phonons in this process through direct measurement of both nonequilibrium phonon and spin dynamics. The momentum- and mode-resolved information in our state-of-the-art MeV UEDS experiments goes beyond simple phenomenological approaches to electron-phonon coupling and reveals the rich temporal dynamics of nonequilibrium phonons in complex materials such as  $\text{MnBi}_2\text{Te}_4$ .

We illustrate that with a sufficiently large  $J_{pd}$ , not only do the miniscule itinerant  $p$ -like magnetic moments ( $\sim 0.05 \mu_B$ ) follow the dynamics of dominant localized Mn  $3d$  magnetic moments ( $\sim 4.3 \mu_B$ ), but that the reverse is also possible, i. e. disordering of the  $p$ -like spins results in a concurrent disordering of the localized  $3d$  spins down to picosecond timescales. We note that this is not always the case. For example, in Gd, an elemental ferromagnet, localized  $4f$  spins ( $7 \mu_B$ ) and itinerant  $5d$  spins ( $0.55 \mu_B$ ) exhibit disparate ultrafast demagnetization timescales, despite a large exchange coupling of 130 meV.<sup>[32]</sup> On the contrary, in dilute magnetic semiconductors (DMS), localized  $d$  spins that are isolated from the initial carrier excitation are found to disorder at timescales comparable to

carrier-lattice thermalization,<sup>[49–51]</sup> notwithstanding the vanishing itinerant magnetic moment, similar to the spin dynamics in  $\text{MnBi}_2\text{Te}_4$  reported here.

Quantized transport phenomena in magnetic topological materials are the consequence of gapping of the TSS by localized magnetic order, which is enabled by  $J_{pd}$  in  $\text{MnBi}_2\text{Te}_4$ . We now consider the consequence of the  $J_{pd}$  on the size of the exchange gap in the TSS of  $\text{MnBi}_2\text{Te}_4$ . Under the assumption of homogeneous, fully saturated localized  $S = 5/2$  spins, A-type AFM order at the surface, our estimated value of  $J_{pd}$  greater than 10 meV implies (using Equation 1) an optimal exchange gap greater than 25 meV. This may be compared to the range of experimentally measured exchange gaps from <2 meV to >60 meV<sup>[15,16,29–31,52,53]</sup>, and theoretical estimates in the range of 30–60 meV.<sup>[15,54]</sup>

A number of explanations have been offered in the literature for the vanishingly small exchange gaps measured in several experiments. Equipped with an experimentally quantified value of  $J_{pd}$ , together with existing ARPES and magnetic measurements, we can comprehensively evaluate these hypotheses. First, a weak  $J_{pd}$  coupling is hypothesized in some studies as the reason for a small exchange gap.<sup>[21,27]</sup> This is definitively ruled out by our results. Some studies propose that surface spin reconstruction and nanometer-scale domains result in a small exchange gap.<sup>[15,16]</sup> However, surface-sensitive measurements indicate that the A-type AFM order persists into the surface layers,<sup>[21,52]</sup> and magnetic domains in  $\text{MnBi}_2\text{Te}_4$  were measured to have dimensions of tens of microns.<sup>[22]</sup> Together with the large value of  $J_{pd}$ , this hypothesis also seems unlikely. Recent ARPES and STM measurements suggest that spatially inhomogeneous point defects influence the local magnetic structure, thus causing sample-dependent variation in the measured exchange gap.<sup>[29–31]</sup> This suggests that largest measured values of the exchange gap in these studies, ~50 meV, are likely

obtained when the probed area is pristine, and free of point defects. This is consistent with our estimate of an optimal exchange gap greater than 25 meV under pristine conditions. Finally, it has been suggested that TSS in  $\text{MnBi}_2\text{Te}_4$  extend into the bulk, either due to a large decay length,<sup>[16,52]</sup> or surface-bulk hybridization,<sup>[28,55]</sup> resulting in a substantially lower effective magnetic moment in the AFM state, and thus a vanishingly small exchange gap. This constraint may be overcome if the interlayer magnetic coupling is FM rather than AFM. Such an interlayer FM coupling was recently achieved in the closely related  $\text{MnBi}_8\text{Te}_{13}$ , hence resulting in a robust net magnetization within the TSS that is independent of decay length.<sup>[56]</sup> ARPES measurements on this material showed a saturated exchange gap of 33 meV,<sup>[56]</sup> which is once again in good agreement with our estimate of the exchange gap based on  $J_{pd}$ .

The strong exchange coupling between localized spins and topological bands quantified in our experiments thus validates the strategy of using localized magnetic order to create magnetic topological phases, in the  $\text{Mn}(\text{Bi,Sb})_{2n}\text{Te}_{3n+1}$  family of materials and beyond. More generally, our study demonstrates how multimodal ultrafast approaches may be used to quantify exchange couplings in complex functional quantum materials interfaced with magnetism.

## Methods

### Crystal growth and characterization

Single crystals of  $\text{MnBi}_2\text{Te}_4$  were grown using a self-flux method as reported elsewhere.<sup>[18,57]</sup> X-ray diffraction was used to check the crystallinity and phase of the crystals. SQUID magnetometry was used to confirm the antiferromagnetic order with a Néel temperature of 24 K. Detailed magneto-transport measurements confirming the high crystal quality can be found in SI Section S1.

### Ultrafast electron diffuse scattering



Ultrafast electron scattering measurements were carried out at the MeV-UED beamline at the SLAC National Laboratory. The technical details of the experimental setup and principles are explained elsewhere.<sup>[58,59]</sup> The sample was excited using 800 nm (1.55 eV), 60 fs pulses, at a fluence of 5 mJ/cm<sup>2</sup>. The high fluence is necessary to produce a sufficiently large pump-induced change in electron scattering. No laser-induced damage was observed in fluence-dependent damage studies, and the signal was repeatable over thousands of cycles. The kinetic energy of the electron bunches is 3.7 MeV and the pulsewidth is ~100 fs. The pump and probe spot sizes were 464×694 μm and ~70 μm.

Measurements were carried out on flakes of average thickness of around 100 nm, exfoliated using an ex-situ transfer stage onto an amorphous Si<sub>3</sub>N<sub>4</sub> membrane. The flakes were protected with an additional layer of amorphous Si<sub>3</sub>N<sub>4</sub> to prevent degradation.

Ultrafast electron diffuse scattering (UEDS) intensities were obtained by averaging over several scans, with individual electron scattering images normalized and aligned to account for electron beam charge and pointing fluctuations, respectively. Time-resolved diffuse scattering intensities were obtained by integrating over appropriate regions of integration and averaged over symmetry-related points in the scattering phase space based on the *R*-3*m* space group of MnBi<sub>2</sub>Te<sub>4</sub>. The pump-induced changes in diffuse scattering intensity were obtained by subtracting diffuse scattering intensity integrated over time delays  $t < 0$  from the time-resolved intensity. Regions with negative pump-induced changes in scattering intensity corresponding to the tails of Bragg peaks were masked using a Heaviside function, to avoid interference with the diffuse scattering.

### Time-resolved magneto-optic Kerr rotation

Time-resolved magneto-optical Kerr effect (MOKE) measurements were carried out using a 1040 nm 200 kHz Spectra-Physics Spirit Yb-based hybrid-fiber laser coupled to a noncollinear optical parametric amplifier. The amplifier produces <50 fs pulses centered at 800 nm (1.55 eV), used as the pump beam. The 1040 nm (1.2 eV) output is converted to white light, centered at 1025 nm with a FWHM of 20 nm, by focusing it inside a YAG (Yttrium Aluminum Garnet) crystal. The white light is subsequently compressed to ~50 fs pulses using a prism compressor pair and used as the probe beam. The pump and the probe beams are aligned to propagate along the [001] axis of the crystal, at near normal incidence. A Wollaston prism is used to separate S- and P-polarized probe beam reflected off the sample surface. The photoinduced Kerr rotation was measured using balanced photodiodes. Details of the Kerr rotation analysis are outlined elsewhere.<sup>[60]</sup>

The samples were placed in a magneto-optical closed-cycle cryostat (Quantum Design OptiCool). Measurements were carried out at a magnetic field of 1 T applied normal to the sample surface (along the [001] direction). The sample temperature was varied from 10 K to 50 K. A pump fluence of  $\sim 100 \mu\text{J}/\text{cm}^2$  was used.

### Time-resolved resonant soft X-ray scattering

Time-resolved resonant soft X-ray scattering measurements were carried out at beamline 4-ID-C at the Advanced Photon Source in Argonne National Laboratory. Optical pulses centered at 1030 nm (1.2 eV) with a pulsewidth of 300 fs at a repetition rate of 108 kHz were used as the pump. Circularly polarized soft X-ray pulses of variable energy (400-2500 eV) with a pulsewidth of  $\sim 90$  ps at a repetition rate of 6.5 MHz were used as the probe. The pump beam was incident at near normal incidence. The probe beam was incident at an angle of  $22.5^\circ$  in a reflection geometry, and the reflected beam was detected using an avalanche photodiode. This angle of incidence is close to the Bragg reflection condition for the (0 0 1.5) peak that corresponds to the doubling of the unit cell with the onset of AFM order, to maximize the magnetic contrast.

The samples were mounted on a flow cryostat in vacuum and measurements were carried out at a temperature of 15 K at zero magnetic field.

### Electronic structure calculations

Density functional theory calculations were carried out using the Vienna Ab Initio Simulation Package (VASP)<sup>[61–65]</sup> with the PBE exchange correlation functional,<sup>[66]</sup> van der Waals correction via the DFT-D3 method with Becke-Jonson damping,<sup>[67,68]</sup> and spin-orbit coupling. An effective Hubbard  $U_{\text{eff}} = U - J = 2$  eV was also added to the Mn 3d states using Dudarev's approach.<sup>[69]</sup> A non-primitive cell containing two Mn atoms was used to obtain the equilibrium geometry of the system with AFM-A magnetic structure. An energy cutoff of 300 eV was used for all calculations. A  $4 \times 4 \times 4$   $\Gamma$ -centered  $k$ -point mesh was used for equilibrium relaxations. The general energy convergence threshold was  $1 \times 10^{-8}$  eV. For structural relaxation, the energy convergence threshold was  $1 \times 10^{-8}$  eV and the force convergence threshold for relaxation was  $1 \times 10^{-5}$  eV/Å. Gaussian smearing with a 0.02 eV width was also used in all relaxation and single-point energy calculations. Projected density of states calculations with and without spin-orbit coupling employed an energy convergence threshold of  $1 \times 10^{-6}$  eV and the tetrahedron smearing method. Supercells for magnetic exchange calculations were generated using VESTA.<sup>[70]</sup>

## Landau-Lifshitz-Gilbert simulations

We consider a system consisting of 1,024,000 sites each possessing a primitive unit cell with a formula of  $\text{MnBi}_2\text{Te}_4$ . We do not distinguish the atoms within a unit cell for simplicity. We simulate the Langevin dynamics of the spins, where the evolution of the localized  $d$  spin  $S_d^i$  and itinerant  $p$  spin  $S_p^i$  of the site  $i$  follow the stochastic LLG equations, i. e.,

$$\frac{dS_d^i}{dt} = -\frac{\gamma_0}{(1+\alpha_d^2)S_d} \left( S_d^i \times H_d^i + \frac{\alpha_d}{S_d} S_d^i \times (S_d^i \times H_d^i) \right) \quad (2)$$

$$\frac{dS_p^i}{dt} = -\frac{\gamma_0}{(1+\alpha_p^2)S_p} \left( S_p^i \times H_p^i + \frac{\alpha_p}{S_p} S_p^i \times (S_p^i \times H_p^i) \right) \quad (3)$$

Here  $t$  is the time,  $\gamma_0$  is the electron gyromagnetic ratio,  $S_d^i$  and  $S_p^i$  are the saturated magnitudes of  $d$  spin and  $p$  spin of site  $i$ , respectively, and  $\alpha_d$  and  $\alpha_p$  are their damping constants. The effective fields  $H_d^i$  and  $H_p^i$  include driving forces from Hamiltonian  $H$  and thermal fluctuations given by white-noise terms, i. e.  $H_d^i = -\partial H / \partial S_d^i + H_{d,\text{noise}}^i$  and  $H_p^i = -\partial H / \partial S_p^i + H_{p,\text{noise}}^i$ .

The Hamiltonian  $H$  is as shown in Equation 1. For simplicity, we only consider a nonzero  $J_d^{ij}$  between a site and each of its 6 nearest in-plane neighbors ( $J_{d,IP}$ ) as well as 6 nearest out-of-plane neighbors ( $J_{d,OOP}$ ).  $J_{d,IP} > 0$  together with  $J_{d,OOP} < 0$  will give rise to an A-type AFM order of the spins at low temperatures. Exchange interactions between  $p$  spins of different sites and that between  $d$  and  $p$  spins of different sites are neglected.

The white-noise terms  $H_{d,\text{noise}}^i$  and  $H_{p,\text{noise}}^i$  are random vectors that fulfill<sup>[71]</sup>

$$\begin{aligned} \langle H_{d,\text{noise}}^i(t) \rangle &= 0, \quad \langle H_{d,\text{noise},m}^i(t_1), H_{d,\text{noise},n}^j(t_2) \rangle = \delta_{ij} \delta_{mn} \delta(t_1 - t_2) 2\alpha_d k_B T_l S_d / \gamma_0 \\ \langle H_{p,\text{noise}}^i(t) \rangle &= 0, \quad \langle H_{p,\text{noise},m}^i(t_1), H_{p,\text{noise},n}^j(t_2) \rangle = \delta_{ij} \delta_{mn} \delta(t_1 - t_2) 2\alpha_p k_B T_e S_p / \gamma_0 \\ \langle H_{d,\text{noise},m}^i(t_1), H_{p,\text{noise},n}^j(t_2) \rangle &= 0 \end{aligned} \quad (4)$$

Here subscripts  $m, n = 1, 2, 3$  indicate the coordinates of a 3-dimensional Cartesian coordinate system,  $k_B$  is the Boltzmann constant,  $T_l$  and  $T_e$  are the lattice and electronic temperatures of a two-temperature model for the lattice and electrons, as determined using the el-ph thermalization time from UEDS measurements.

The material constants used in the simulation are  $S_d = 2.5$ ,  $S_p = 0.01S_d = 0.025$ ,  $\alpha_d = 0.003$ ,  $\alpha_p = 0.5$ ,  $\gamma_0 = 1.761 \times 10^{11} \text{ T}^{-1} \text{ s}^{-1}$ ,  $J_{d,IP} = 0.16 \text{ meV}$ ,  $J_{d,OP} = -0.022 \text{ meV}$ ,  $K_d = 0.05 \text{ meV}$ , and  $J_{pd} = 10\text{-}200 \text{ meV}$  (see SI Section S10 for details)

## Supporting Information

Supporting Information is available from the Wiley Online Library or from the author.

## Acknowledgements

H.P., V.A.S., H.W., P.K., M.P., N.Z.K., A.M.L., R.D.A., J.M.R., J.W.F., and V.G. acknowledge primary support from the DOE-BES grant DE-SC0012375. The computational efforts on the ultrafast electron scattering experiments and Landau-Lifshitz-Gilbert modeling of ultrafast spin dynamics were supported by the DOE-BES Computational Materials Science program under grant number DE-SC0020145 (H.P., T.Y., L-Q.C., and V.G.). Support for crystal growth and characterization was provided by the National Science Foundation through the Penn State 2D Crystal Consortium-Materials Innovation Platform (2DCC-MIP) under NSF cooperative agreement DMR-1539916. D.P. was supported by the Army Research Office (ARO) under grant no. W911NF-15-1-0017. SLAC MeV-UED is supported in part by the DOE BES SUF Division Accelerator & Detector R&D program, the LCLS Facility, and SLAC under Contract Nos. DE-AC02-05-CH11231 and DE-AC02-76SF00515.

H.P., V.A.S., and V.G. conceived the project. H.P., V.A.S., H.W., X.S., A.H.R., M-F.L., S.P., A.M.L., V.G., and X.W. carried out the ultrafast electron diffuse scattering measurements at the SLAC National Laboratory. P.K., M.P., H.P., R.A., and V.G. carried out the magneto-optic Kerr rotation measurements. V.A.S. and J.W.F. carried out the resonant soft X-ray scattering measurements in Argonne National Laboratory. S-H.L. and Z.M. synthesized single crystals of  $\text{MnBi}_2\text{Te}_4$  used in the measurements. L.M. and H.P. carried out the SQUID magnetometry measurements. T.Y. and L-Q.C. carried out the LLG simulations. N.K., D.P., and J.M.R. carried out the density functional theory simulations. A.B.G. carried out the calculations for the minimal theoretical model. H.P. analyzed the experimental results with inputs from all authors. H.P. wrote the manuscript with inputs from all authors.

The authors declare no competing interests.

Received: ((will be filled in by the editorial staff))

Revised: ((will be filled in by the editorial staff))

Published online: ((will be filled in by the editorial staff))

## References

- [1] M. M. Otrokov, I. I. Klimovskikh, H. Bentmann, D. Estyunin, A. Zeugner, Z. S. Aliev, S. Gaß, A. U. B. Wolter, A. V. Koroleva, A. M. Shikin, M. Blanco-Rey, M. Hoffmann, I. P. Rusinov, A. Y. Vyazovskaya, S. V. Ereemeev, Y. M. Koroteev, V. M. Kuznetsov, F. Freyse, J. Sánchez-Barriga, I. R. Amiraslanov, M. B. Babanly, N. T. Mamedov, N. A. Abdullayev, V. N. Zverev, A. Alfonsov, V. Kataev, B. Büchner, E. F. Schwier, S. Kumar, A. Kimura, L. Petaccia, G. Di Santo, R. C. Vidal, S. Schatz, K. Kißner, M. Ünzelmann, C. H. Min, S. Moser, T. R. F. Peixoto, F. Reinert, A. Ernst, P. M. Echenique, A. Isaeva, E. V. Chulkov, *Nature* **2019**, 576, 416.
- [2] J. Wu, F. Liu, M. Sasase, K. Ienaga, Y. Obata, R. Yukawa, K. Horiba, H. Kumigashira, S. Okuma, T. Inoshita, H. Hosono, *Sci. Adv.* **2019**, 5, eaax9989.
- [3] S. H. Lee, D. Graf, L. Min, Y. Zhu, H. Yi, S. Ciocys, Y. Wang, E. S. Choi, R. Basnet, A. Fereidouni, A. Wegner, Y.-F. Zhao, K. Verlinde, J. He, R. Redwing, V. Gopalan, H. O. H. Churchill, A. Lanzara, N. Samarth, C.-Z. Chang, J. Hu, Z. Q. Mao, *Phys. Rev. X* **2021**, 11, 031032.
- [4] E. D. L. Rienks, S. Wimmer, J. Sánchez-Barriga, O. Caha, P. S. Mandal, J. Růžička, A. Ney, H. Steiner, V. V. Volobuev, H. Groiss, M. Albu, G. Kothleitner, J. Michalička, S. A. Khan, J. Minár, H. Ebert, G. Bauer, F. Freyse, A. Varykhalov, O. Rader, G. Springholz, *Nature* **2019**, 576, 423.
- [5] B. Chen, F. Fei, D. Zhang, B. Zhang, W. Liu, S. Zhang, P. Wang, B. Wei, Y. Zhang, Z. Zuo, J. Guo, Q. Liu, Z. Wang, X. Wu, J. Zong, X. Xie, W. Chen, Z. Sun, S. Wang, Y. Zhang, M. Zhang, X. Wang, F. Song, H. Zhang, D. Shen, B. Wang, *Nat. Commun.* **2019**, 10, 4469.
- [6] S. Wimmer, J. Sánchez-Barriga, P. Küppers, A. Ney, E. Schierle, F. Freyse, O. Caha, J. Michalička, M. Liebmann, D. Primetzhofer, M. Hoffman, A. Ernst, M. M. Otrokov, G. Bihlmayer, E. Weschke, B. Lake, E. V. Chulkov, M. Morgenstern, G. Bauer, G. Springholz, O. Rader, *Adv. Mater.* **2021**, 33, 2102935.
- [7] Y. Deng, Y. Yu, M. Z. Shi, Z. Guo, Z. Xu, J. Wang, X. H. Chen, Y. Zhang, *Science*. **2020**, 367, 895.
- [8] C. Liu, Y. Wang, H. Li, Y. Wu, Y. Li, J. Li, K. He, Y. Xu, J. Zhang, Y. Wang, *Nat. Mater.* **2020**, 19, 522.

This article is protected by copyright. All rights reserved.

- [9] H. Deng, Z. Chen, A. Wołoś, M. Konczykowski, K. Sobczak, J. Sitnicka, I. V Fedorchenko, J. Borysiuk, T. Heider, Ł. Pluciński, K. Park, A. B. Georgescu, J. Cano, L. Krusin-Elbaum, *Nat. Phys.* **2021**, *17*, 36.
- [10] Y. Tokura, K. Yasuda, A. Tsukazaki, *Nat. Rev. Phys.* **2019**, *1*, 126.
- [11] H. Zhang, C. Liu, X. Qi, X. Dai, Z. Fang, S. Zhang, *Nat. Phys.* **2009**, *5*, 438.
- [12] A. S. Núñez, J. Fernández-Rossier, *Solid State Commun.* **2012**, *152*, 403.
- [13] Q. Liu, C.-X. Liu, C. Xu, X.-L. Qi, S.-C. Zhang, *Phys. Rev. Lett.* **2009**, *102*, 156603.
- [14] R. Yu, W. Zhang, H.-J. Zhang, S.-C. Zhang, X. Dai, Z. Fang, *Science*. **2010**, *329*, 61.
- [15] Y.-J. Hao, P. Liu, Y. Feng, X.-M. Ma, E. F. Schwier, M. Arita, S. Kumar, C. Hu, R. Lu, M. Zeng, Y. Wang, Z. Hao, H.-Y. Sun, K. Zhang, J. Mei, N. Ni, L. Wu, K. Shimada, C. Chen, Q. Liu, C. Liu, *Phys. Rev. X* **2019**, *9*, 041038.
- [16] Y. J. Chen, L. X. Xu, J. H. Li, Y. W. Li, H. Y. Wang, C. F. Zhang, H. Li, Y. Wu, A. J. Liang, C. Chen, S. W. Jung, C. Cacho, Y. H. Mao, S. Liu, M. X. Wang, Y. F. Guo, Y. Xu, Z. K. Liu, L. X. Yang, Y. L. Chen, *Phys. Rev. X* **2019**, *9*, 041040.
- [17] J.-Q. Yan, Q. Zhang, T. Heitmann, Z. Huang, K. Y. Chen, J.-G. Cheng, W. Wu, D. Vaknin, B. C. Sales, R. J. McQueeney, *Phys. Rev. Mater.* **2019**, *3*, 064202.
- [18] S. H. Lee, Y. Zhu, Y. Wang, L. Miao, T. Pillsbury, H. Yi, S. Kempinger, J. Hu, C. A. Heikes, P. Quarterman, W. Ratcliff, J. A. Borchers, H. Zhang, X. Ke, D. Graf, N. Alem, C.-Z. Chang, N. Samarth, Z. Mao, *Phys. Rev. Res.* **2019**, *1*, 12011.
- [19] B. Li, J.-Q. Yan, D. M. Pajerowski, E. Gordon, A.-M. Nedić, Y. Sizyuk, L. Ke, P. P. Orth, D. Vaknin, R. J. McQueeney, *Phys. Rev. Lett.* **2020**, *124*, 167204.
- [20] B. Li, D. M. Pajerowski, S. X. M. Riberolles, L. Ke, J.-Q. Yan, R. J. McQueeney, *Phys. Rev. B* **2021**, *104*, L220402.
- [21] P. M. Sass, J. Kim, D. Vanderbilt, J. Yan, W. Wu, *Phys. Rev. Lett.* **2020**, *125*, 037201.
- [22] P. M. Sass, W. Ge, J. Yan, D. Obeysekera, J. J. Yang, W. Wu, *Nano Lett.* **2020**, *20*, 2609.
- [23] J. S. Dyck, P. Hájek, P. Lošťák, C. Uher, *Phys. Rev. B* **2002**, *65*, 115212.

- [24] F. Matsukura, H. Ohno, A. Shen, Y. Sugawara, *Phys. Rev. B* **1998**, *57*, R2037.
- [25] M. Köpf, J. Ebad-Allah, S. H. Lee, Z. Q. Mao, C. A. Kuntscher, *Phys. Rev. B* **2020**, *102*, 165139.
- [26] A. Zeugner, F. Nietschke, A. U. B. Wolter, S. Gaß, R. C. Vidal, T. R. F. Peixoto, D. Pohl, C. Damm, A. Lubk, R. Hentrich, S. K. Moser, C. Fornari, C. H. Min, S. Schatz, K. Kißner, M. Ünzelmann, M. Kaiser, F. Scaravaggi, B. Rellinghaus, K. Nielsch, C. Hess, B. Büchner, F. Reinert, H. Bentmann, O. Oeckler, T. Doert, M. Ruck, A. Isaeva, *Chem. Mater.* **2019**, *31*, 2795.
- [27] H. Li, S.-Y. Gao, S.-F. Duan, Y.-F. Xu, K.-J. Zhu, S.-J. Tian, J.-C. Gao, W.-H. Fan, Z.-C. Rao, J.-R. Huang, J.-J. Li, D.-Y. Yan, Z.-T. Liu, W.-L. Liu, Y.-B. Huang, Y.-L. Li, Y. Liu, G.-B. Zhang, P. Zhang, T. Kondo, S. Shin, H.-C. Lei, Y.-G. Shi, W.-T. Zhang, H.-M. Weng, T. Qian, H. Ding, *Phys. Rev. X* **2019**, *9*, 041039.
- [28] C. Yan, S. Fernandez-Mulligan, R. Mei, S. H. Lee, N. Protic, R. Fukumori, B. Yan, C. Liu, Z. Mao, S. Yang, *Phys. Rev. B* **2021**, *104*, L041102.
- [29] A. M. Shikin, D. A. Estyunin, I. I. Klimovskikh, S. O. Filnov, E. F. Schwier, S. Kumar, K. Miyamoto, T. Okuda, A. Kimura, K. Kuroda, K. Yaji, S. Shin, Y. Takeda, Y. Saitoh, Z. S. Aliev, N. T. Mamedov, I. R. Amiraslanov, M. B. Babanly, M. M. Otrokov, S. V. Eremeev, E. V. Chulkov, *Sci. Rep.* **2020**, *10*, 13226.
- [30] A. M. Shikin, D. A. Estyunin, N. L. Zaitsev, D. Glazkova, I. I. Klimovskikh, S. O. Filnov, A. G. Rybkin, E. F. Schwier, S. Kumar, A. Kimura, N. Mamedov, Z. Aliev, M. B. Babanly, K. Kokh, O. E. Tereshchenko, M. M. Otrokov, E. V. Chulkov, K. A. Zvezdin, A. K. Zvezdin, *Phys. Rev. B* **2021**, *104*, 115168.
- [31] M. Garnica, M. M. Otrokov, P. C. Aguilar, I. I. Klimovskikh, D. Estyunin, Z. S. Aliev, I. R. Amiraslanov, N. A. Abdullayev, V. N. Zverev, M. B. Babanly, N. T. Mamedov, A. M. Shikin, A. Arnau, A. L. V. de Parga, E. V. Chulkov, R. Miranda, *npj Quantum Mater.* **2022**, *7*, 7.
- [32] B. Frietsch, J. Bownan, R. Carley, M. Teichmann, S. Wienholdt, D. Hinzke, U. Nowak, K. Carva, P. M. Oppeneer, M. Weinelt, *Nat. Commun.* **2015**, *6*, 8262.
- [33] B. Frietsch, A. Donges, R. Carley, M. Teichmann, J. Bownan, K. Döbrich, K. Carva, D. Legut, P. M. Oppeneer, U. Nowak, M. Weinelt, *Sci. Adv.* **2020**, *6*, eabb1601.
- [34] I. Radu, K. Vahaplar, C. Stamm, T. Kachel, N. Pontius, H. A. Dürr, T. A. Ostler, J. Barker, R. F. L. Evans, R. W. Chantrell, A. Tsukamoto, A. Itoh, A. Kirilyuk, T. Rasing, A. V. Kimel, *Nature* **2011**,

472, 205.

- [35] H. Padmanabhan, M. Poore, P. K. Kim, N. Z. Koocher, V. A. Stoica, D. Puggioni, H. (Hugo) Wang, X. Shen, A. H. Reid, M. Gu, M. Wetherington, S. H. Lee, R. D. Schaller, Z. Mao, A. M. Lindenberg, X. Wang, J. M. Rondinelli, R. D. Averitt, V. Gopalan, *Nat. Commun.* **2022**, *13*, 1929.
- [36] H.-P. Sun, C. M. Wang, S.-B. Zhang, R. Chen, Y. Zhao, C. Liu, Q. Liu, C. Chen, H.-Z. Lu, X. C. Xie, *Phys. Rev. B* **2020**, *102*, 241406.
- [37] R. J. Elliott, *Phys. Rev.* **1954**, *96*, 266.
- [38] Y. Yafet, in *Solid State Phys.* (Eds.: F. Seitz, D. Turnbull), Academic Press, **1963**.
- [39] B. Koopmans, G. Malinowski, F. Dalla Longa, D. Steiauf, M. Fähnle, T. Roth, M. Cinchetti, M. Aeschlimann, *Nat. Mater.* **2010**, *9*, 259.
- [40] J. A. Tomko, S. Kumar, R. Sundararaman, P. E. Hopkins, *J. Appl. Phys.* **2021**, *129*, 193104.
- [41] J. K. Chen, W. P. Latham, J. E. Beraun, *J. Laser Appl.* **2005**, *17*, 63.
- [42] Z. Lin, L. V. Zhigilei, V. Celli, *Phys. Rev. B* **2008**, *77*, 075133.
- [43] F. Dalla Longa, *Laser-Induced Magnetization Dynamics : An Ultrafast Journey among Spins and Light Pulses*, Technische Universiteit Eindhoven, **2008**.
- [44] B. A. Bernevig, T. L. Hughes, S.-C. Zhang, *Science*. **2006**, *314*, 1757.
- [45] C.-Z. Chang, J. Zhang, M. Liu, Z. Zhang, X. Feng, K. Li, L.-L. Wang, X. Chen, X. Dai, Z. Fang, X.-L. Qi, S.-C. Zhang, Y. Wang, K. He, X.-C. Ma, Q.-K. Xue, *Adv. Mater.* **2013**, *25*, 1065.
- [46] X. Kou, M. Lang, Y. Fan, Y. Jiang, T. Nie, J. Zhang, W. Jiang, Y. Wang, Y. Yao, L. He, K. L. Wang, *ACS Nano* **2013**, *7*, 9205.
- [47] J.-Q. Yan, S. Okamoto, M. A. McGuire, A. F. May, R. J. McQueeney, B. C. Sales, *Phys. Rev. B* **2019**, *100*, 104409.
- [48] J. G. Checkelsky, J. Ye, Y. Onose, Y. Iwasa, Y. Tokura, *Nat. Phys.* **2012**, *8*, 729.
- [49] J. Wang, C. Sun, Y. Hashimoto, J. Kono, G. A. Khodaparast, Ł. Cywiński, L. J. Sham, G. D. Sanders, C. J. Stanton, H. MuneKata, *J. Phys. Condens. Matter* **2006**, *18*, R501.



- [50] J. Wang, C. Sun, J. Kono, A. Oiwa, H. MuneKata, Ł. Cywiński, L. J. Sham, *Phys. Rev. Lett.* **2005**, 95, 167401.
- [51] J. Wang, Ł. Cywiński, C. Sun, J. Kono, H. MuneKata, L. J. Sham, *Phys. Rev. B* **2008**, 77, 235308.
- [52] D. Nevola, H. X. Li, J.-Q. Yan, R. G. Moore, H.-N. Lee, H. Miao, P. D. Johnson, *Phys. Rev. Lett.* **2020**, 125, 117205.
- [53] H.-R. Ji, Y.-Z. Liu, H. Wang, J.-W. Luo, J.-H. Li, H. Li, Y. Wu, Y. Xu, J. Wang, *Chinese Phys. Lett.* **2021**, 38, 107404.
- [54] J. Li, Y. Li, S. Du, Z. Wang, B.-L. Gu, S.-C. Zhang, K. He, W. Duan, Y. Xu, *Sci. Adv.* **2019**, 5, eaaw5685.
- [55] X.-M. Ma, Z. Chen, E. F. Schwier, Y. Zhang, Y.-J. Hao, S. Kumar, R. Lu, J. Shao, Y. Jin, M. Zeng, X.-R. Liu, Z. Hao, K. Zhang, W. Mansuer, C. Song, Y. Wang, B. Zhao, C. Liu, K. Deng, J. Mei, K. Shimada, Y. Zhao, X. Zhou, B. Shen, W. Huang, C. Liu, H. Xu, C. Chen, *Phys. Rev. B* **2020**, 102, 245136.
- [56] R. Lu, H. Sun, S. Kumar, Y. Wang, M. Gu, M. Zeng, Y.-J. Hao, J. Li, J. Shao, X.-M. Ma, Z. Hao, K. Zhang, W. Mansuer, J. Mei, Y. Zhao, C. Liu, K. Deng, W. Huang, B. Shen, K. Shimada, E. F. Schwier, C. Liu, Q. Liu, C. Chen, *Phys. Rev. X* **2021**, 11, 011039.
- [57] S. H. Lee, D. Graf, L. Min, Y. Zhu, H. Yi, S. Ciocys, Y. Wang, E. S. Choi, R. Basnet, A. Fereidouni, A. Wegner, Y. F. Zhao, K. Verlinde, J. He, R. Redwing, V. Gopalan, H. O. H. Churchill, A. Lanzara, N. Samarth, C. Z. Chang, J. Hu, Z. Q. Mao, *Phys. Rev. X* **2021**, 11, 31032.
- [58] S. P. Weathersby, G. Brown, M. Centurion, T. F. Chase, R. Coffee, J. Corbett, J. P. Eichner, J. C. Frisch, A. R. Fry, M. Gühr, N. Hartmann, C. Hast, R. Hettel, R. K. Jobe, E. N. Jongewaard, J. R. Lewandowski, R. K. Li, A. M. Lindenberg, I. Makasyuk, J. E. May, D. McCormick, M. N. Nguyen, A. H. Reid, X. Shen, K. Sokolowski-Tinten, T. Vecchione, S. L. Vetter, J. Wu, J. Yang, H. A. Dürr, X. J. Wang, *Rev. Sci. Instrum.* **2015**, 86, 073702.
- [59] X. Shen, R. K. Li, U. Lundström, T. J. Lane, A. H. Reid, S. P. Weathersby, X. J. Wang, *Ultramicroscopy* **2018**, 184, 172.
- [60] D. J. Lovinger, E. Zoghlin, P. Kissin, G. Ahn, K. Ahadi, P. Kim, M. Poore, S. Stemmer, S. J. Moon, S. D. Wilson, R. D. Averitt, *Phys. Rev. B* **2020**, 102, 085138.

- [61] G. Kresse, J. Hafner, *Phys. Rev. B* **1994**, 49, 14251.
- [62] G. Kresse, J. Furthmüller, *Comput. Mater. Sci.* **1996**, 6, 15.
- [63] G. Kresse, J. Furthmüller, *Phys. Rev. B* **1996**, 54, 11169.
- [64] G. Kresse, J. Hafner, *Phys. Rev. B* **1993**, 47, 558.
- [65] G. Kresse, D. Joubert, *Phys. Rev. B* **1999**, 59, 1758.
- [66] J. P. Perdew, K. Burke, M. Ernzerhof, *Phys. Rev. Lett.* **1996**, 77, 3865.
- [67] S. Grimme, J. Antony, S. Ehrlich, H. Krieg, *J. Chem. Phys.* **2010**, 132, 154104.
- [68] S. Grimme, S. Ehrlich, L. Goerigk, *J. Comput. Chem.* **2011**, 32, 1456.
- [69] S. Dudarev, G. Botton, *Phys. Rev. B* **1998**, 57, 1505.
- [70] K. Momma, F. Izumi, *J. Appl. Crystallogr.* **2011**, 44, 1272.
- [71] U. Nowak, in *Handb. Magn. Adv. Magn. Mater.*, John Wiley & Sons, Ltd, **2007**.

Magnetic topological materials rely on strong interaction between localized spins and states comprising the topological bands. This interaction is directly interrogated for the first time in an intrinsic magnetic topological material,  $\text{MnBi}_2\text{Te}_4$  using a multimodal ultrafast approach. It is found that this exchange coupling is  $>100$  times stronger than the superexchange interaction, implying an optimal exchange gap of  $>25$  meV.

Hari Padmanabhan\*, Vladimir A. Stoica, Peter Kim, Maxwell Poore, Tiannan Yang, Xiaozhe Shen, Alexander H. Reid, Ming-Fu Lin, Suji Park, Jie Yang, Huaiyu Wang, Nathan Z. Koocher, Danilo Puggioni, Alexandru B. Georgescu, Lujin Min, Seng-Huat Lee, Zhiqiang Mao, James M. Rondinelli, Aaron M. Lindenberg, Long-Qing Chen, Xijie Wang, Richard D. Averitt, John W. Freeland, and Venkatraman Gopalan\*

### Large Exchange Coupling Between Localized Spins and Topological Bands in Magnetic Topological Insulator $\text{MnBi}_2\text{Te}_4$

